



Explaining Spectral Line Profiles in the Horsehead Nebula Using Cloud Surface Curvature

Student
Ducheng Lu

Supervisors
Franck Le Petit (LERMA)
Emeric Bron (LERMA)

Jan 2025

Contents

1	Introduction	2
1.1	Photodissociation Regions (PDRs)	2
1.2	The Horsehead Nebula	3
2	Data	4
3	Methods	5
3.1	The MeudonPDR code	5
3.1.1	Constant Pressure vs. Constant Density	5
3.1.2	Models with Exact Radiative Transfer of H ₂	6
3.1.3	Models with Surface Chemistry	8
3.2	Modeling Column Densities in Spherical Geometry	9
3.3	Solving the Radiative Transfer Equation	10
3.4	Convolution of Line Profiles with Instrumental Resolution	11
4	Results and Discussion	12
4.1	Convolved Column Densities from Spherical Geometry Model	12
4.2	Effect of Cloud Radius on Column Densities	13
4.3	Line Profiles with Radiative Transfer	14
5	Conclusions	14

Abstract

Context.

Aim.

Methods.

Results.

Abstract

Contexte.

Objectif.

Méthodes.

Résultats.

1 Introduction

The interstellar medium (ISM) is composed of gas and dust between stars in galaxies. The ISM is site of star formation and takes up around $\sim 10\%$ of total baryonic mass (Draine 2011). In return, the radiation field produced by stars is responsible for the heating the gas and dust that cool in bright line and continuum emission. These emission lines provide information about the physical conditions inside the ISM, such as the temperature, density and chemical composition.

Models have long been developed to help us interpret these

The 1D slab geometry may not be appropriate in some cases, and the curvature of the PDR region needs to be taken into account in order to reproduce the line profiles. A common technique is to use a time-dependent hydrodynamic simulation to obtain the density and velocity fields and then to postprocess it with a PDR code to obtain the steady-state chemical abundances and thermal equilibrium gas temperature (e.g., Levrier et al. 2012).

In this project, I aim to develop a wrapper for the MeudonPDR code code that can take the output of the slab geometry model and compute the column density in spherical geometry. I will also consider the radiative transfer of the lines.

1.1 Photodissociation Regions (PDRs)

Photodissociation regions (PDRs) are regions where far-ultraviolet (FUV; $6\text{ eV} < h\nu < 13.6\text{ eV}$) radiation dominates the chemical or heating processes (Tielens and Hollenbach 1985). PDRs span a wide range of incident FUV fluxes and densities, including all neutral gas in the interstellar medium (ISM) and molecular layers where FUV radiation drives molecule formation.

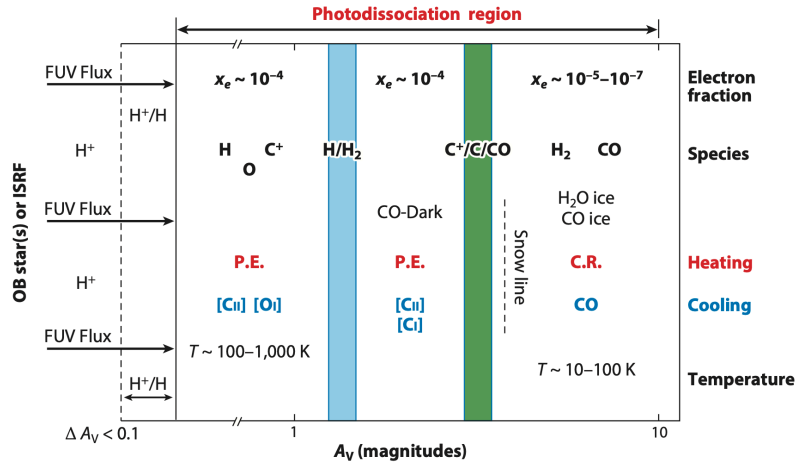


Figure 1: Schematic of a photodissociation region as a function of visual extinction A_V . Reprinted from Wolfire et al. (2022), Fig. 2. Red text indicates the dominant heating mechanisms, with "P.E." referring to photoelectric effects and "C.R." referring to cosmic rays. Blue text represents the main line emissions, which are the main cooling mechanisms.

PDRs are the primary sources of infrared (IR) line and continuum radiation in galaxies (Crawford et al. 1985; Stacey et al. 2010). Grains absorb the majority of the FUV radiation and re-radiate it in the IR continuum, but a fraction of the FUV photons heat the gas, which then cool through line emission. Together, the line and continuum emission provide important insights into the physical and chemical conditions in PDRs. The study of PDRs

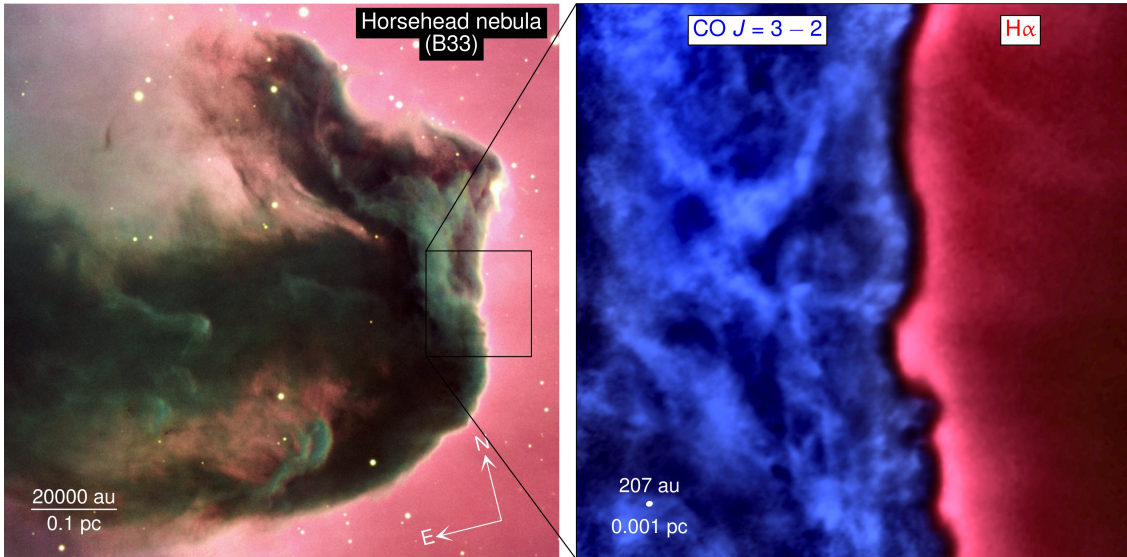


Figure 2: Multiphase view of the Horsehead nebula (Barnard 33). Reprinted from Hernández-Vera et al. (2023). Left: Composite color image of the Horsehead nebula observed with the VLT (ESO). Right: Zoomed-in view of the edge of the molecular cloud, imaged with ALMA in the CO $J = 3 - 2$ line emission (blue) and the 0.9 m KPNO telescope in the $H\alpha$ line emission. The dark region represents the neutral atomic layer.

is vital for understanding star formation and galaxy evolution. Observations of PDRs help to constrain key physical parameters such as temperature, chemical composition, and radiative energy, probing the local environments of star-forming regions and the potential presence of stellar feedback.

Fig. 1 shows a one-dimensional (1D) structure of PDR illuminated by radiation field from the left. The adjacent H_{II} region absorbs extreme-ultraviolet (EUV; $h\nu > 13.6$ eV) photons, leaving FUV photons that create the PDR. Atomic hydrogen, helium, and oxygen are neutral because their ionization potentials exceed 13.6 eV, while molecules are photodissociated, and metals like carbon, silicon, and sulfur are singly ionized. The heating process is dominated by photoelectric effects on small grains and polycyclic aromatic hydrocarbons (PAHs), and the cooling process is dominated by fine-structure line emission. As the depth increases and FUV radiation diminishes, H_2 forms, followed by CO. Both H_2 and CO photodissociate via line absorption and can therefore self-shield, allowing them to form closer to the surface than other molecules like H_2O or O_2 , which dissociate via FUV continuum. In the deepest layers, cosmic rays dominate the heating process, and rotational transitions of CO become the primary coolants.

1.2 The Horsehead Nebula

The Horsehead Nebula (Fig. 2 and cover image) is a well-known PDR that has been extensively studied in the literature. It is illuminated by σ Orionis, a O9.5V binary star system (Warren and Hesser 1977), located 3.5 pc from the edge of the PDR (Abergel et al. 2003; Schirmer et al. 2020), resulting in an incident radiation field of around $2.7 \times 10^{-3} \text{ erg s}^{-1} \text{ cm}^{-2}$ (Habart et al. 2005).

In observational studies, it is customary to use arcseconds as the distance unit. As the Horsehead PDR is located approximately 400 pc from us (Menten et al. 2007; Schlafly

et al. 2014), the distance unit can be converted as:

$$\alpha["] = \frac{d[\text{pc}]}{400 \text{ pc}} \frac{1''}{1 \text{ rad}}. \quad (1)$$

This gives $1''$ corresponding to 1.9 mpc. The horsehead PDR is nearly edge-on, with an upper limit for the angle of 6° (Habart et al. 2005).

For lines that are optically thin, the local emissivity is given by

$$\epsilon_{ul} \simeq \frac{1}{4\pi} A_{ul} n_u h\nu_{ul} \propto n_u \quad (2)$$

2 Data

The observational data used in this study (Fig. 3) were obtained from the Heterodyne Instrument for the Far-Infrared (HIFI) (de Graauw et al. 2010) onboard the Herschel Space Observatory (Pilbratt et al. 2010). All data are convolved to the spatial resolution of the HIFI H₂O data, 38.1 arcsec. The observed molecular species were detected at specific wavelengths corresponding to transitions listed in Table 1.

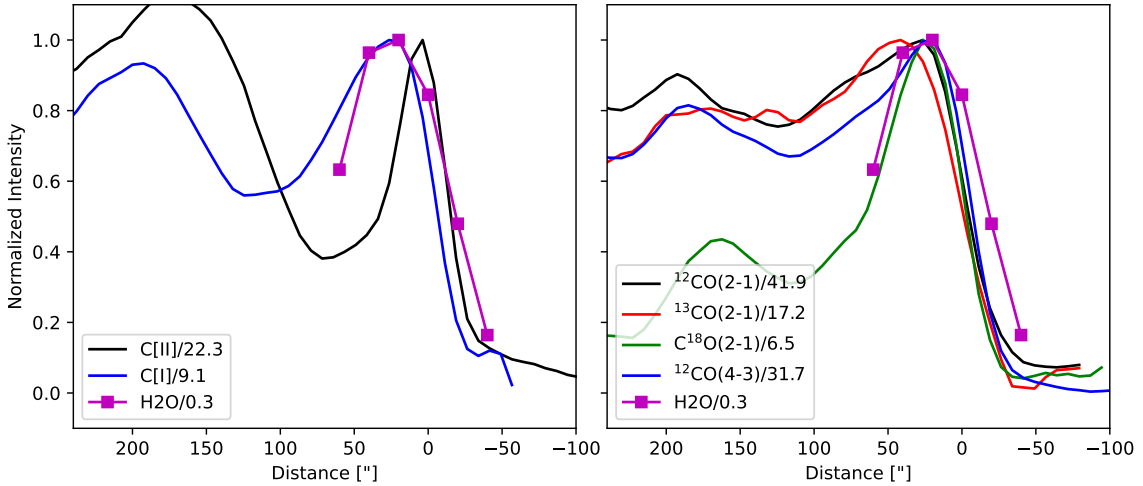


Figure 3: Observed line profiles of the Horsehead Nebula by Herschel HIFI. Reproduced from [cite the original paper](#). The ^{13}CO lines has been removed due to bad weather condition during the observation.

Notation	Species	Upper Level	Lower Level	Frequency (GHz)
H ₂ O	H ₂ O	J=1, Ka=1, Kc=0	J=1, Ka=0, Kc=1	557.30
C[II]	C ⁺	2P J=3/2	2P J=1/2	1902.59
C[I]	C	3P J=1	3P J=0	492.02
¹² CO (2-1)	CO	v=0, J=2	v=0, J=1	230.538
¹² CO (4-3)	CO	v=0, J=4	v=0, J=3	461.041
¹³ CO (2-1)	¹³ CO	v=0, J=2	v=0, J=1	220.399
C ¹⁸ O (2-1)	C ¹⁸ O	v=0, J=2	v=0, J=1	219.560

Table 1: Parameters of transitions in the observation data used in this study.

3 Methods

3.1 The MeudonPDR code

A significant heterogeneity exists among the available PDR models, which differ in their geometry, physical and chemical structures, and model parameters. Röllig et al. (2007) suggest that the choice of a specific code should depend on the physical and chemical processes implemented in the code, as well as the characteristics of the emission source.

In this project, I used the MeudonPDR code (Bron 2014; Bron et al. 2014, 2016; Goicoechea and Le Bourlot 2007; Gonzalez Garcia et al. 2008; Le Bourlot et al. 2012; Le Petit et al. 2006) to simulate the Horsehead Nebula. The MeudonPDR code models a stationary one-dimensional (1D) slab of gas and dust illuminated by an ultraviolet (UV) radiation field from one or both sides (Fig. 4). At each iteration, the code solves the UV radiative transfer in both the continuum and lines, followed by the chemical balance, and finally the level populations and thermal balance. The code outputs the level populations, the gas temperature, and the chemical abundances as a function of the depth into the cloud, with optional output of the radiation field. The physical parameters used to model the Horsehead PDR are summarized in Table 2.

Cloud size ($A_{V,\max}^{(1)}$)	40
Proton density ⁽²⁾ (n_H)	$3 \times 10^4 - 3 \times 10^6 \text{ cm}^{-3}$
Pressure ⁽²⁾ (P)	$1 \times 10^6 - 1 \times 10^7 \text{ K cm}^{-3}$
ISRF	shape: Mathis ⁽³⁾ , geometry: beam_isot ⁽⁴⁾
ISRF scaling factor	$G_0^{\text{obs}} = 100$, $G_0^{\text{back}} = 0.04^{(5)}$
UV radiative transfer method	FGK approximation, or exact H ₂ self- and mutual shielding ⁽⁶⁾
Turbulent velocity dispersion	$2 \text{ km s}^{-1(7)}$
Extinction Curve	HD38087 ⁽⁸⁾
$R_V = A_V/E(B - V)$	5.50
$C_D = N_H/E(B - V)$	1.57×10^{22}

Table 2: Key physical parameters used to model the Horsehead PDR in the MeudonPDR code.¹Visual extinction, $A_V \equiv 2.5 \log_{10}(I_V^0/I_V^{\text{obs}})$. ²Proton density is used in constant density models, and pressure is used in constant pressure models(see Sec. 3.1.1). ³Mathis et al. (1983). ⁴Perpendicular on observer side, isotropic on back side. ⁵In Habing units, as defined in Le Petit et al. (2006). ⁶ See Sec. 3.1.2. ⁷Only used in Doppler line broadening. ⁸Fitzpatrick and Massa (1990). Other parameters use default values. More descriptions can be found in the MeudonPDR documentation.

3.1.1 Constant Pressure vs. Constant Density

The density structure of a PDR model, whether it assumes constant density, constant pressure, or a user-defined density profile, can significantly influence the simulation results (Wolfire et al. 2022). As shown in Fig. 5 and Fig. 6, I compare the cloud structure computed with constant pressure and constant density assumptions, illustrating the differences in the resulting PDR structures. The values $n_H = 3 \times 10^5 \text{ cm}^{-3}$ for the constant density model and $P = 5 \times 10^6 \text{ K cm}^{-3}$ for the constant pressure model are based on Maillard (2023). In the constant pressure model, the transition from atomic to molecular hydrogen occurs at higher visual extinction (Fig. 5), and the total physical thickness

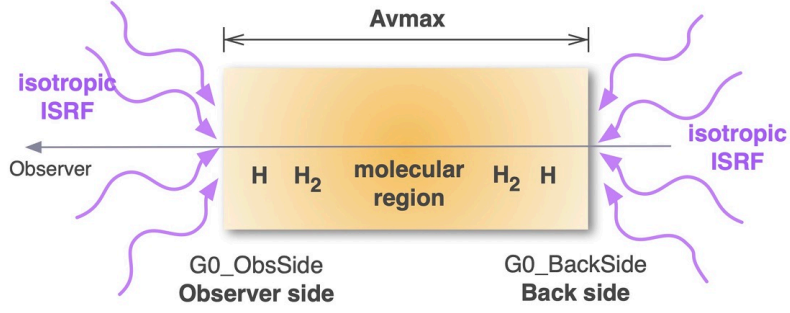


Figure 4: Scheme of the slab geometry in MeudonPDR code. $A_V = 0$ at the observer side and increases toward the back side, reaching $A_V = A_{V,\text{max}}$, which controls the size of the cloud. Reprinted from Fig. 3.1 in MeudonPDR documentation.

of the cloud is larger (Fig. 6). The temperature profile in the constant pressure model is also more gradual. Additional comparisons between various constant density models and constant pressure models are provided in the appendix.

Observations of the Horsehead Nebula reveal a steep density gradient in the PDRs (Guzmán et al. 2011; Habart et al. 2005). Hernández-Vera et al. (2023) showed that constant density models fail to reproduce the observed structures, and neither do previously proposed density profile prescriptions. Furthermore, recent observations from ALMA and Herschel indicate that the warm layer of PDRs is indeed isobaric, with by relatively high thermal pressures (Bron et al. 2018; Goicoechea et al. 2016; Joblin et al. 2018; Mailard et al. 2021; Marconi et al. 1998; Wu et al. 2018). Based on these findings, I adopt a constant pressure model with $P = 5 \times 10^6 \text{ K cm}^{-3}$ for the subsequent analysis.

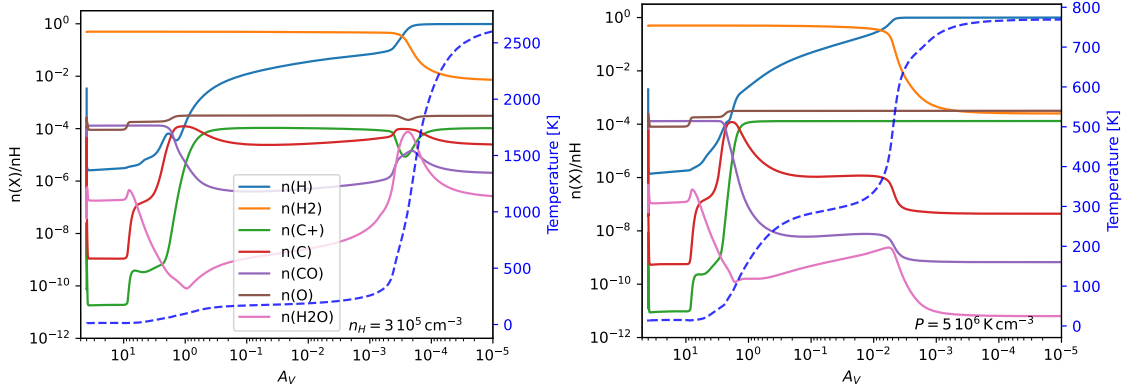


Figure 5: Comparison of the cloud structure computed with constant density $n_H = 3 \times 10^5 \text{ cm}^{-3}$ (left) and constant pressure $P = 5 \times 10^6 \text{ K cm}^{-3}$ (right), with a shared legend displayed in the left plot. All other parameters are the same as those listed in Table. 2.

3.1.2 Models with Exact Radiative Transfer of H_2

There are two options available in the MeudonPDR code for treating radiative transfer in the UV. The first is the FGK approximation (Federman et al. 1979), in which the self-shielding of H and H_2 molecules is treated approximately. Self-shielding occurs when molecules absorb radiation in their own spectral lines, reducing the flux available to penetrate deeper into the cloud. However, the FGK approximation neglects mutual shielding, where the overlap and interaction of absorption lines between different species or multiple lines of the same species further attenuate the radiation field.

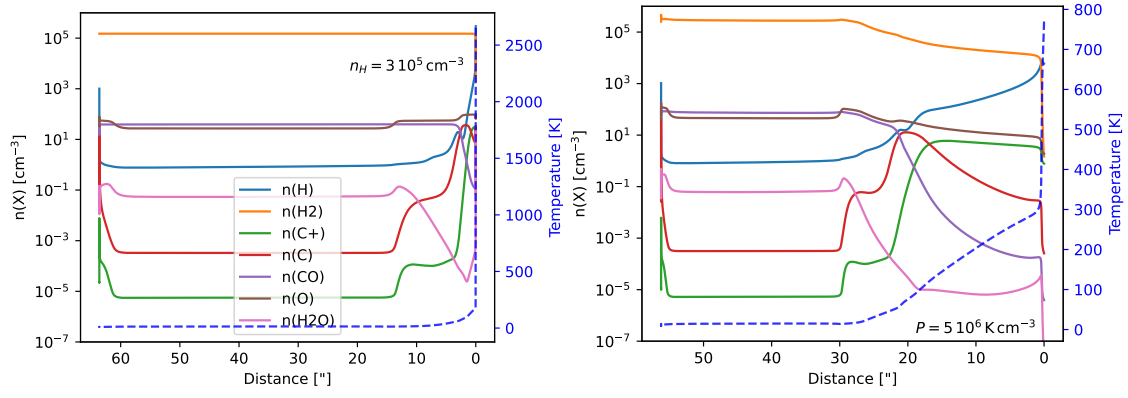


Figure 6: Similar to Fig. 5, but using physical units, with arcseconds as the distance unit and the densities represented by their actual values (not normalized by proton density).

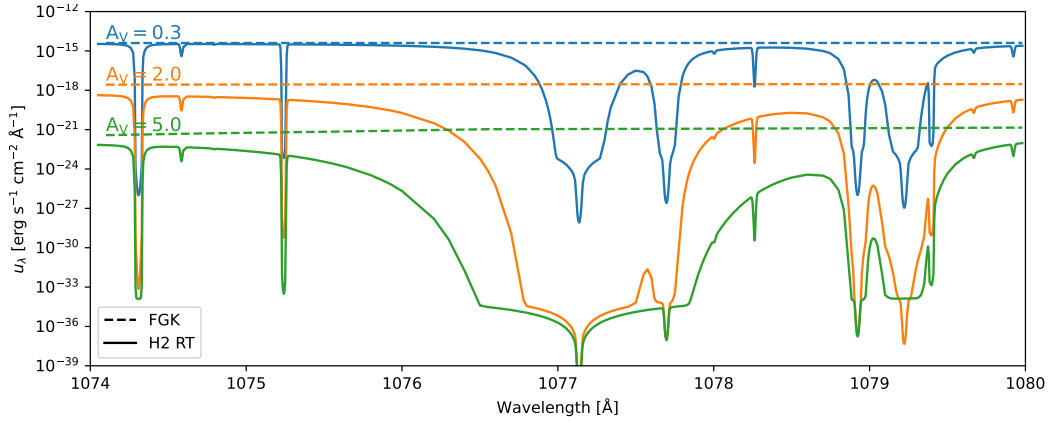


Figure 7: Comparison of the local energy density of the radiation field from 1074 Å to 1080 Å at visual extinction depths $A_V = 0.3$ (blue), $A_V = 2$ (orange), and $A_V = 5$ (green), for models computed using the FGK approximation (dashed lines) and the exact radiative transfer method (solid lines) including the 20 lowest H_2 absorption lines.

The second, more accurate approach is to solve the radiative transfer exactly. This method explicitly includes mutual shielding for a given number of energy levels of H , H_2 , D , HD , CO , ^{13}CO , and $C^{18}O$, as detailed in Goicoechea and Le Bourlot (2007) and Gonzalez Garcia et al. (2008). For higher energy levels, the FGK approximation is retained, as their contributions are negligible due to their low populations.

Fig. 7 compares spectra from 1074 Å to 1080 Å at various visual extinction values for models computed using the FGK approximation and the exact radiative transfer method, demonstrating pronounced attenuation when applying the exact method of H_2 radiative transfer. Although computationally more intensive, the exact method enables a more accurate treatment of the UV radiation field, which subsequently influences the PDR structure. For instance, the exact method leads to increased attenuation of the radiation field, shifting the H/H_2 transition layer to lower extinction depths (Goicoechea and Le Bourlot 2007), as illustrated in Fig. 8. Furthermore, the enhanced attenuation from mutual shielding results in a lower temperature profile. To balance accuracy and computational efficiency, my model applies exact radiative transfer only to the 20 lowest energy levels of H_2 , which are the primary contributors to the attenuation. **how to explain the second bump occurring in the both cases?**

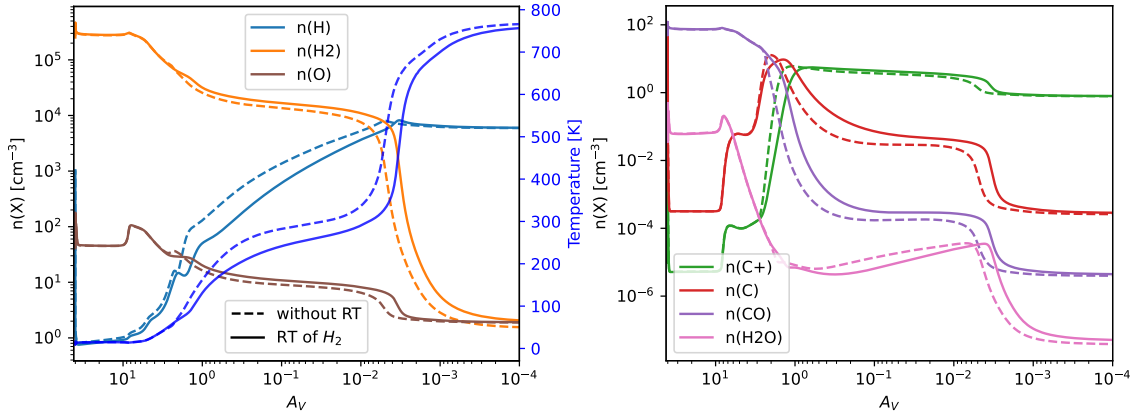


Figure 8: Comparison of temperature profile and abundances for models computed with (solid) and without (dashed) exact radiative transfer (RT) of H_2 : H species and O (left), and C species, CO, and H_2O (right).

3.1.3 Models with Surface Chemistry

In the ISM, direct gas-phase formation of molecules is very inefficient. Instead, molecules are formed on the surfaces of dust grains, which act as catalysts by providing a surface for adsorbed atoms to meet and react. The grains also absorb the excess energy released by the formation process, preventing dissociation that would otherwise occur in the gas-phase formation. The formation of H_2 is a key demonstration of the importance of this process, as the gas-phase formation rate of H_2 is much lower than the rate required to explain the observed abundance of H_2 in the ISM (Gould and Salpeter 1963; Hollenbach and Salpeter 1971). In addition to chemical reactions, dust grains also play a role in the sublimation and freeze-out of molecules, leading to “jumps” or “drops” in molecular profiles at specific temperatures (Herbst and van Dishoeck 2009).

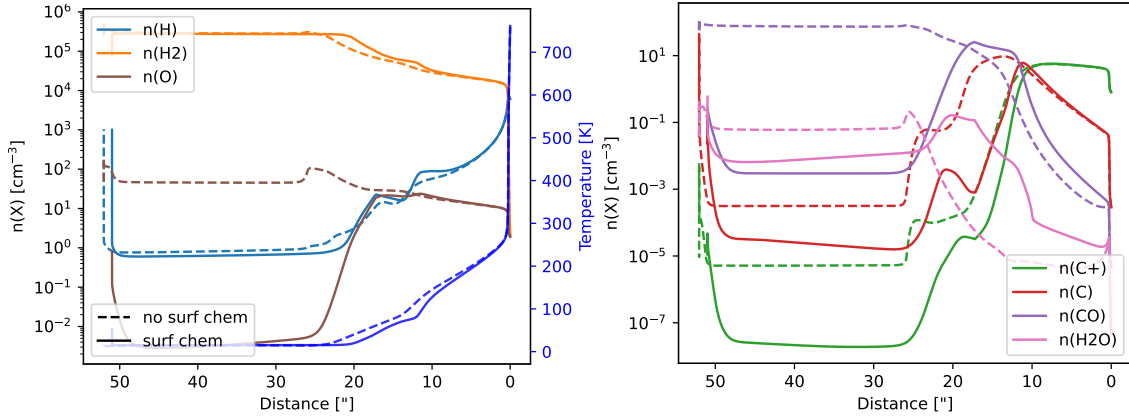


Figure 9: Comparison of temperature profile and abundances for models computed with (solid lines) and without (dashed lines) surface chemistry: H species and O (left), and C species, CO, and H_2O (right).

In Fig. 9, I compare the PDR models computed with and without surface chemistry. The inclusion of surface reactions leads to an earlier rise in the abundances of $n(\text{H}_2)$, $n(\text{CO})$ and $n(\text{H}_2\text{O})$ due to enhanced production on dust grain surfaces. At greater depths within the cloud, the abundances of almost all molecules decrease in the model with surface chemistry because of the freeze-out of molecules onto the dust grains. Grains also reduce the gas temperature, as they absorb the energy released during molecule formation, as shown in the left panel. Therefore, including surface chemistry in PDR models is

crucial for accurately describing the molecular abundances and the gas temperature.

To summarize the model comparisons in this section, I will use the constant pressure model with exact radiative transfer of H_2 and surface chemistry to consider the curvature of the cloud's surface in the following sections.

3.2 Modeling Column Densities in Spherical Geometry

To model the curvature of the cloud, I treat the PDR region as the outermost shell of a fictitious spherical cloud, assuming plane-parallel geometry, as shown in Fig. 10. This approximation is valid when the curvature radius of the cloud's surface is relatively small compared to the radius of the cloud. For the models in this study, the physical depth of the PDR region is approximately 0.08 pc, which is significantly smaller than the curvature radius, as seen in Fig. 2, thereby justifying the use of plane-parallel geometry. Under this assumption, I consider all physical variables at a given distance from the cloud's surface to be equal to those computed by the MeudonPDR code model at the same distance from the cloud's edge.

The radius R of the fictitious spherical cloud is provided as an input parameter to the wrapper code. A line of sight (LoS) is defined by its impact parameter b , which measures the perpendicular distance from the LoS to the center of the cloud. From the output of the MeudonPDR code, the level number densities $n_X(d)$ are obtained as a function of the depth d into the cloud. In plane-parallel geometry, $n_X(d)$ gives the number density at a point located at a depth d from the spherical surface.

The column density along a given LoS is determined by interpolating the number density at each depth d and then integrating along the LoS. To do this, I first compute the range of distances inside the PDR region along the LoS. The maximum half-distance s_{\max} is given by:

$$s_{\max} = \sqrt{R^2 - b^2}, \quad (3)$$

while the computation of the minimum half-distance s_{\min} depends on whether the LoS penetrates beyond the PDR region (see Fig. 10):

$$s_{\min} = \begin{cases} 0 & \text{if } b > R - d_{\text{PDR}}, \text{ LoS 1} \\ \sqrt{(R - d_{\text{PDR}})^2 - b^2} & \text{if } b < R - d_{\text{PDR}}, \text{ LoS 2} \end{cases}, \quad (4)$$

where d_{PDR} is the depth of the PDR region. Next, the distance s along the LoS is converted into the depth d from the cloud's surface. Using Pythagorean theorem, one can easily establish that $d = R - \sqrt{s^2 + b^2}$. The number density at each point along the LoS is then calculated as:

$$n_X(s) = f(R - \sqrt{s^2 + b^2}), \quad (5)$$

where $f(d)$ is the interpolated function of the level number density $n_X(d)$. Finally, the column density $N_X(b)$ for a given LoS with impact parameter b is obtained by integrating the number density along the LoS. By symmetry, the total column density is twice the integral over the half-LoS:

$$N_X(b) = 2 \int_{s_{\min}}^{s_{\max}} n_X(s') ds'. \quad (6)$$

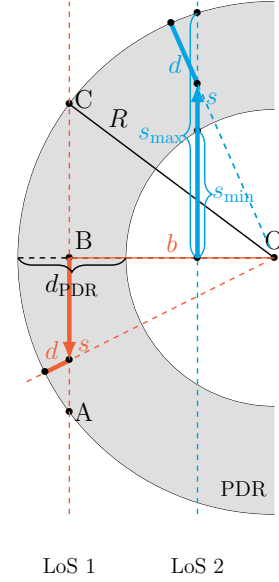


Figure 10: Scheme of the spherical, plane-parallel geometry. Curvature exaggerated for clarity.

By considering the curvature of the cloud's surface, this column density allows for a more direct comparison with observations. However, this approach does not account for the absorption and emission processes occurring inside the cloud. For lines that are optically thick, the radiative transfer equation must be solved along the LoS to accurately reproduce the observed line profiles. This more detailed treatment will be addressed in the next section.

3.3 Solving the Radiative Transfer Equation

In the previous calculation of the column densities, I assumed that all lines were optically thin. However, some lines can be optically thick, leading to differences in the observed line profiles for various lines, as seen in Fig 3. To account for line extinction within the cloud, I need to solve the radiative transfer equation along the LoS (see, e.g., Rybicki and Lightman 1979, Eq. 1.67):

$$\frac{dI_\nu}{ds} = A_{ul}n_u \frac{h\nu}{4\pi} \phi(\nu) + B_{ul}n_u \frac{h\nu}{4\pi} I_\nu \phi(\nu) - B_{lu}n_l \frac{h\nu}{4\pi} I_\nu \phi(\nu), \quad (7)$$

where n_u and n_l are the number densities of the upper and lower levels of the transition, respectively, h is the Planck's constant, ν is the frequency of the transition, and $\phi(\nu)$ is the line profile. For simplicity, I use the same line profile for both emission and absorption, neglecting scattering. **justify?**

The coefficients A_{ul} , B_{ul} , B_{lu} in Eq. 7 are the Einstein coefficients for spontaneous emission, stimulated emission, and absorption, respectively. These coefficients are intrinsic properties of the specific transition and are related through the Einstein relations (Einstein 1917):

$$B_{ul} = \frac{c^2}{2h\nu_{ul}^3} A_{ul}, \quad g_l B_{lu} = g_u B_{ul}, \quad (8)$$

where g_u and g_l are the degeneracies of the upper and lower levels.

In PDRs, the motion of atoms and molecules results in line broadening. Thermal motion produces a Gaussian profile, while microturbulent motions contribute an additional broadening component. The thermal and turbulent broadening effects are combined in the effective Doppler width, $\Delta\nu_D$, which is then included in the Gaussian line profile (see, e.g., Rybicki and Lightman 1979, Eqs. 10.68-10.72):

$$\phi(\nu) = \frac{1}{\sigma_\nu \sqrt{2\pi}} \exp\left(-\frac{(\nu - \nu_0)^2}{2\sigma_\nu^2}\right), \quad (9)$$

where

$$\sigma_\nu = \frac{\sqrt{2}}{2} \Delta\nu_D, \quad \Delta\nu_D = \frac{\nu_0}{c} \sqrt{\frac{2kT}{m} + v_{\text{turb}}^2}. \quad (10)$$

Here, ν_0 is the central frequency of the transition, c is the speed of light, T is the gas temperature, m is the mass of the emitting species, and $v_{\text{turb}} = 2 \text{ km s}^{-1}$ is the turbulent velocity, as introduced in Table. 2.

The line profile is normalized so that $\int_0^\infty \phi(\nu) d\nu = 1$. To ensure computational efficiency while maintaining a good representation of the profile, I truncate the line profile at 5σ . Therefore, in practice, the normalization becomes $\int_{\nu_0-5\sigma}^{\nu_0+5\sigma} \phi(\nu) d\nu = 1$. **if have time, add a figure to demonstrate that this is reasonable for the lines concerned?**

To solve the radiative transfer equation, I also need a background intensity I_0 . For this, I use the isotropic specific intensity on the observer side, as provided by the MeudonPDR

code in the file `_IncRadField.dat`. It is important to note that the current implementation is valid only for isotropic radiation; handling more general forms of background specific intensity would require additional modifications. **add explanation why?**

The external radiation field in the `IncRadField.dat` file is provided in units of $\text{erg}/\text{cm}^2/\text{s}/\text{sr}/\text{\AA}$. However, to solve the radiative transfer equation, I need the specific intensity in units of $\text{erg}/\text{cm}^2/\text{s}/\text{sr}/\text{Hz}$. By energy conservation, $I_\nu |d\nu| = I_\lambda |d\lambda|$, and using $c = \lambda\nu$, I can derive the differential relation $d\lambda = -c/\nu^2 d\nu$. This allows me to convert between the two sets of units as follows:

$$I_\nu = I_\lambda \left| \frac{d\lambda}{d\nu} \right| = I_\lambda \frac{c}{\nu^2} = I_\lambda \frac{\lambda^2}{c}. \quad (11)$$

Thus far, we have focused on improving the modeling of the physical processes in PDRs. However, the observed spectra are inevitably influenced by the resolution of the instrument used for observation. The instrumental resolution effectively smooths out the line profile, broadening the observed lines and altering their shapes. Consequently, it is essential to account for the instrument's resolution in the modeling process. In the following section, I will discuss the convolution process and how it modifies the observed spectra.

3.4 Convolution of Line Profiles with Instrumental Resolution

The spatial resolution of an instrument is typically characterized by its point spread function (PSF), which describes the response of the instrument to a point source. To account for the effects of instrumental resolution on the observed line profiles, I convolve the model's line profile with the PSF. Since the spatial grid provided by MeudonPDR code is non-uniform, I first interpolate it onto a uniform and monotonic grid.

The PSF is often approximated as a Gaussian function. For this work, the Gaussian kernel is expressed as:

$$g(x) = \frac{1}{\sqrt{2\pi}} \exp\left(-\frac{x^2}{2\sigma^2}\right), \quad (12)$$

where x is the distance from the center of the PSF, and σ is the standard deviation of the Gaussian. The standard deviation σ is related to the full width half maximum (FWHM) of the instrument by $\sigma = \text{FWHM} / (2\sqrt{2 \ln 2})$.

To reduce computational cost, I truncate the Gaussian PSF at 3σ , as the contribution from points beyond this range is negligible. The PSF is then normalized over the truncated range to conserve total intensity, with the normalization constant $K = \sum_{x=-3\sigma}^{3\sigma} g(x) \Delta x$, where Δx is the spacing of the uniform grid.

The convolution of the line profile, $f(x)$, with the normalized PSF is performed as:

$$(f * g)(x) = \frac{1}{K} \sum_{\tau=x_{\min}-3\sigma}^{x_{\max}+3\sigma} F(\tau) g(x - \tau) \Delta x, \quad (13)$$

where x_{\min} and x_{\max} define the bounds of the spatial grid, and $F(\tau)$ is the value of the line profile at point τ .

Fig. 11 or Fig. 17? illustrates how convolution alters the line profile. The convolved profiles demonstrate how increasing the FWHM progressively smooths the line profile, reducing peak intensity and redistributing the signal over a broader spatial range.

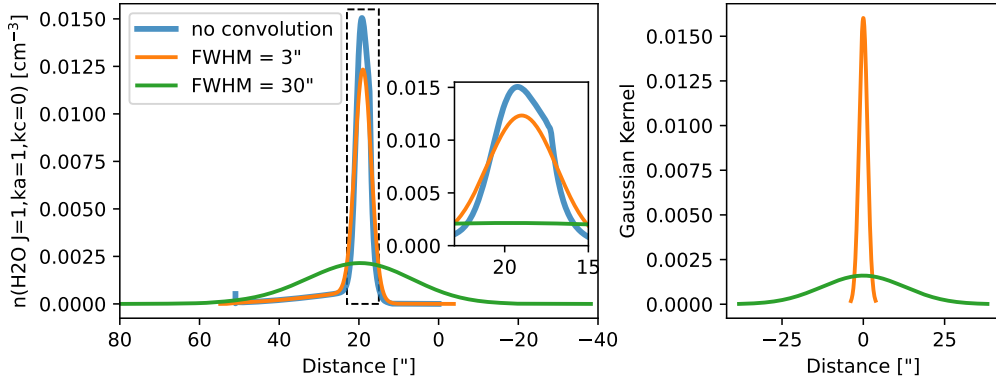


Figure 11: Illustration of the Convolution Process. The left panel shows the original line profile (blue) alongside the profiles convolved with Gaussian PSFs of resolutions 3'' (orange) and 30'' (green), with a zoomed-in view of the area within the dashed rectangle. The right panel shows the corresponding Gaussian PSFs, normalized and truncated at 3σ .

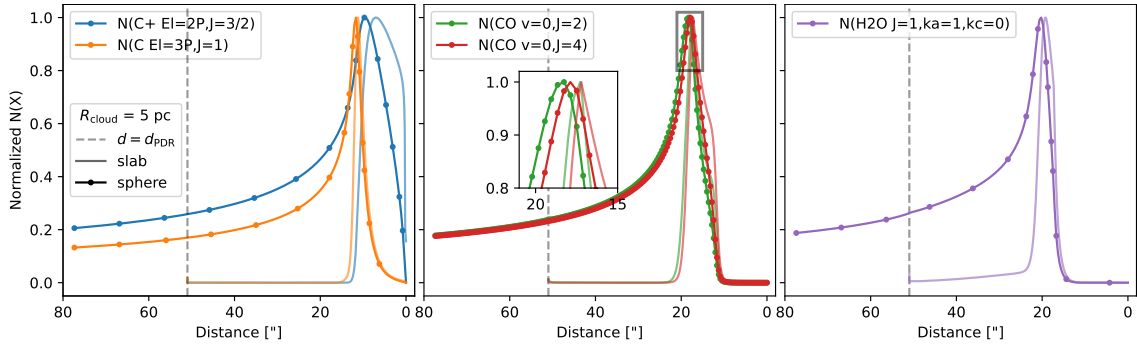


Figure 12: Comparison of normalized column density profiles for slab geometry (solid lines) and spherical geometry (solid lines with dots) with a cloud radius of $R_{\text{cloud}} = 5 \text{ pc}$. In Panel 1, $N(\text{C}^+ \text{ 2P, } J=3/2)$ (blue) and $N(\text{C 3P, } J=1)$ (orange) are shown; in Panel 2, $N(\text{CO } v=0, J=2)$ (green) and $N(\text{CO } v=0, J=4)$ (red); and in Panel 3, $N(\text{H}_2\text{O } J=1, k_a=1, k_c=0)$ (purple). The dashed gray lines indicate the maximum depth of the PDR model, d_{PDR} . The rectangle marks the zoomed-in region in Panel 2.

4 Results and Discussion

4.1 Convolved Column Densities from Spherical Geometry Model

In Secs. 3.2 and 3.4, I described the modeling of spherical geometry using the wrapper for the MeudonPDR code and the convolution of line profiles with the instrumental resolution. In this section, I present the convolved column density profiles for the spherical geometry model with a cloud radius of $R_{\text{cloud}} = 5 \text{ pc}$. Comparisons are made first between the spherical and slab geometry models, then between the unconvolved and convolved profiles, and finally between the convolved profiles and the observational data.

Fig. 12 compares the profiles from the spherical geometry model with those from the slab geometry model. In the spherical geometry model, the curvature of the cloud's surface causes the PDR layer to bend away from the tangent at the cloud's surface, in contrast to the slab geometry, where the PDR layer is directly at the surface. As a result, the PDR layer reaches greater depths in the spherical geometry, producing a more extended profile. Additionally, the peaks shift to deeper locations within the cloud, as the line of sight (LoS) passing through the greatest distance within the emitting region is slightly behind the emitting region. When convolution is applied, the line profiles are smoothed

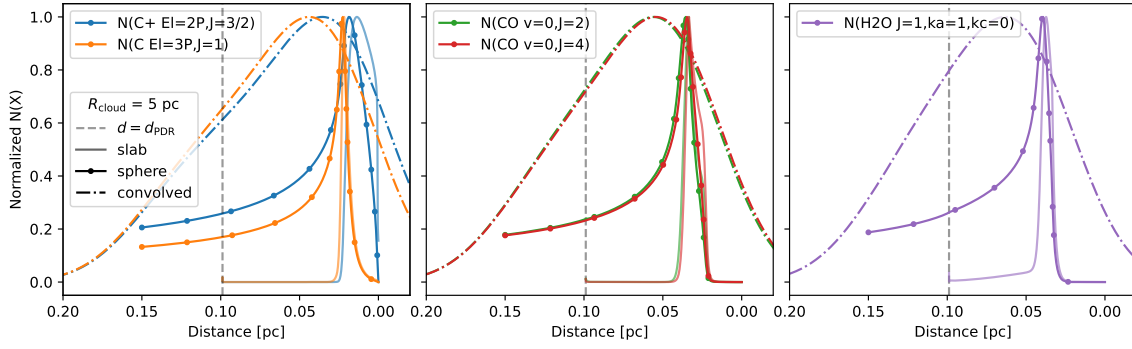


Figure 13: Similar to Fig. 12, but with the addition of convolved column densities (dashed-dotted lines), alongside the profiles for slab geometry (solid lines) and spherical geometry (solid lines with dots).

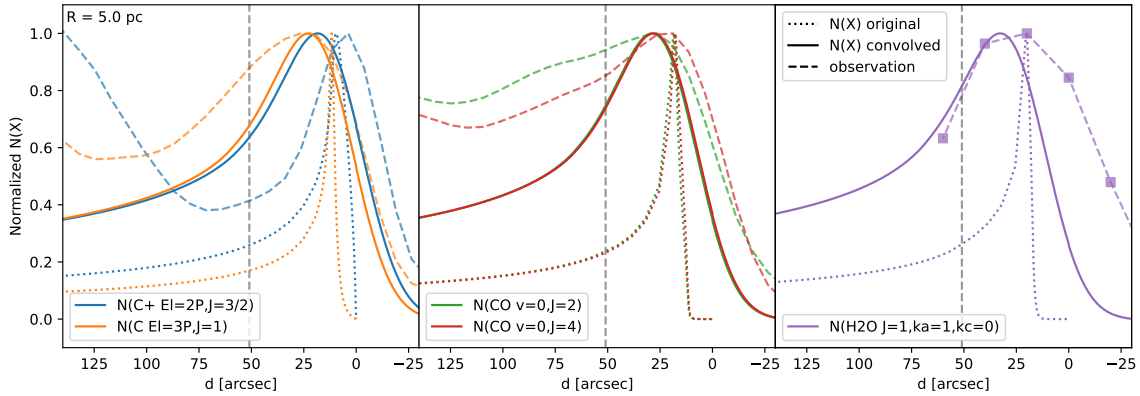


Figure 14: Comparison of column density profiles for a model with spherical geometry ($R_{\text{cloud}} = 5 \text{ pc}$, solid lines) and observations (dashed lines). The unconvolved profiles (dotted lines) are also shown for comparison.

and further extended (Fig. 13), with the peaks shifting to greater depths. The convex tail behind the emitting region disappears, yielding a more Gaussian-like shape.

The convolved profiles provide a closer match to the observed data, as shown in Fig. 14, particularly in terms of the shape and extent of the profiles. This suggests that the inclusion of curvature and convolution improves the modelling of the observed column density profiles. In the following section, I investigate how varying the cloud radius affects the column density profiles.

4.2 Effect of Cloud Radius on Column Densities

There are no significant changes to the rising side of the profiles or the locations of the peaks with varying cloud radius R_{cloud} . Instead, variations in R_{cloud} primarily affect the shape of the profile's tail (Fig. 15). As the cloud radius increases, the surface curvature decreases, making the emitting region more tangent to the LoS at the same depth from the cloud's surface. This reduces the passage length and, consequently, causes the tail to decline more steeply.

None of the models reproduce the observed profiles accurately. A direct comparison, with profiles overlapped to emphasize differences in shape, is provided in Fig. 18 in the appendix. Notably, the observed profiles exhibit significant variation in the tail shape, whereas the modeled profiles remain quite similar. This discrepancy is likely due to the lack of a detailed treatment of radiative transfer in the models, as mentioned in Sec. 3.3, which we will address in the next section.

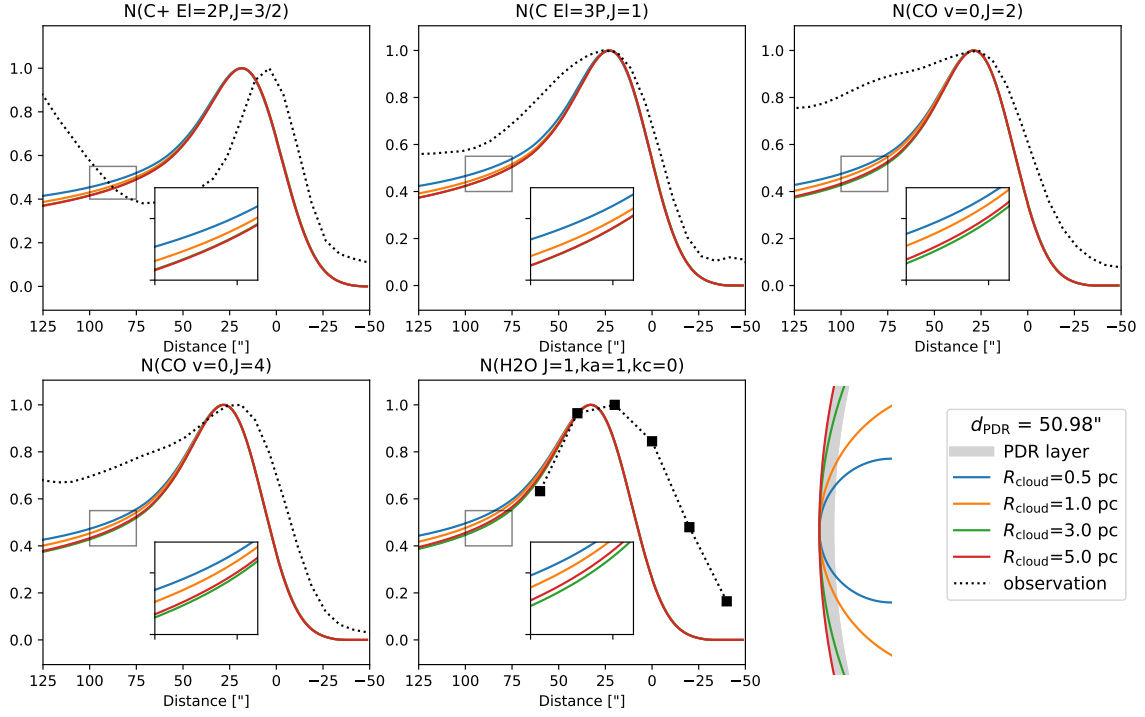


Figure 15: Comparison of normalized line profiles for different cloud radii: $R_{\text{cloud}} = 0.5$ pc (blue), 1.0 pc (orange), 3.0 pc (green), and 5.0 pc (red). Observations are shown as dotted lines. A schematic representation of the cloud radii is included in the bottom right corner. The areas marked by black rectangles are shown with greater detail in zoomed-in views.

4.3 Line Profiles with Radiative Transfer

To validate the solver, we test it by solving the radiative transfer equation with constant density profiles for both the lower and upper levels. In this case, the radiative transfer equation simplifies to:

$$\frac{dI_\nu}{ds} = c_1 + c_2 I_\nu, \quad (14)$$

where $c_1 = A_{ul}n_u\phi(\nu)h\nu/4\pi$ and $c_2 = (B_{ul}n_u - B_{lu}n_l)\phi(\nu)h\nu/4\pi$ are constants. The analytical solution to this equation is:

$$I_\nu(s) = (I_0 + \frac{c_1}{c_2})e^{c_2 s} - \frac{c_1}{c_2}. \quad (15)$$

For this toy problem, we solve the radiative transfer equation for the CO transition from $v = 0, J = 2$ to $v = 0, J = 1$, assuming constant density profiles of $n_u = 2 \text{ cm}^{-3}$ and $n_l = 2 \text{ cm}^{-3}$. The computed results are compared with the analytical solution in Fig. 16.

Due to time constraints, I was unable to fully implement the method discussed in Sec. 3.3. Specifically, my results are limited to solving the radiative transfer equation at the line center, without taking into account the line-broadening profile, $\phi(\nu)$. Despite this limitation, the implemented methods illustrate how solving the radiative transfer equation along the LoS affects the shape of the profiles. Future work could build on these results by incorporating the full line-broadening profile and comparing the results with observed data.

5 Conclusions

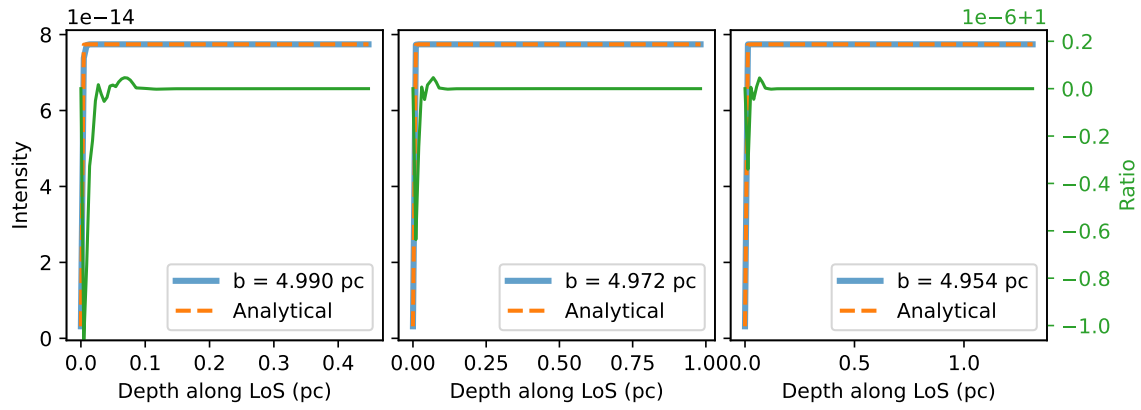


Figure 16: Comparison of the computed (blue solid lines) and analytical (orange dashed lines) solutions to the radiative transfer equation for the CO transition from $v = 0, J = 2$ to $v = 0, J = 1$ along LoS with different impact parameters in a 5 pc cloud. The right axes show the ratio between the numerical solution and the analytical one.

References

- Abergel, A. et al. (2003). “ISOCAM and molecular observations of the edge of the Horse-head nebula”. In: *A&A* 410, pp. 577–585. DOI: [10.1051/0004-6361:20030878](https://doi.org/10.1051/0004-6361:20030878).
- Bron, E. (2014). “Stochastic processes in the interstellar medium”. 2014PA077169. PhD thesis, 1 vol. (382 p.)
- Bron, E., Le Bourlot, J., and Le Petit, F. (2014). “Surface chemistry in the interstellar medium. II. H_2 formation on dust with random temperature fluctuations”. In: *A&A* 569, A100, A100. DOI: [10.1051/0004-6361/201322101](https://doi.org/10.1051/0004-6361/201322101).
- Bron, E., Le Petit, F., and Le Bourlot, J. (2016). “Efficient ortho-para conversion of H_2 on interstellar grain surfaces”. In: *A&A* 588, A27, A27. DOI: [10.1051/0004-6361/201527879](https://doi.org/10.1051/0004-6361/201527879).
- Bron, E. et al. (2018). “Photoevaporating PDR models with the Hydra PDR Code”. In: *arXiv e-prints*, arXiv:1801.01547, arXiv:1801.01547. DOI: [10.48550/arXiv.1801.01547](https://doi.org/10.48550/arXiv.1801.01547).
- Crawford, M. K. et al. (1985). “Far-infrared spectroscopy of galaxies : the 158 micron $C+$ line and the energy balance of molecular clouds.” In: *ApJ* 291, pp. 755–771. DOI: [10.1086/163113](https://doi.org/10.1086/163113).
- de Graauw, T. et al. (2010). “The Herschel-Heterodyne Instrument for the Far-Infrared (HIFI)”. In: *A&A* 518, L6, p. L6. DOI: [10.1051/0004-6361/201014698](https://doi.org/10.1051/0004-6361/201014698).
- Draine, B. T. (2011). *Physics of the Interstellar and Intergalactic Medium*.
- Einstein, A. (1917). “Zur Quantentheorie der Strahlung”. In: *Physikalische Zeitschrift* 18, pp. 121–128.
- Federman, S. R., Glassgold, A. E., and Kwan, J. (1979). “Atomic to molecular hydrogen transition in interstellar clouds.” In: *ApJ* 227, pp. 466–473. DOI: [10.1086/156753](https://doi.org/10.1086/156753).
- Fitzpatrick, E. L. and Massa, D. (1990). “An Analysis of the Shapes of Ultraviolet Extinction Curves. III. an Atlas of Ultraviolet Extinction Curves”. In: *ApJS* 72, p. 163. DOI: [10.1086/191413](https://doi.org/10.1086/191413).
- Goicoechea, J. R. and Le Bourlot, J. (2007). “The penetration of Far-UV radiation into molecular clouds”. In: *A&A* 467.1, pp. 1–14. DOI: [10.1051/0004-6361:20066119](https://doi.org/10.1051/0004-6361:20066119).
- Goicoechea, J. R. et al. (2016). “Compression and ablation of the photo-irradiated molecular cloud the Orion Bar”. In: *Nature* 537.7619, pp. 207–209. DOI: [10.1038/nature18957](https://doi.org/10.1038/nature18957).

- Gonzalez Garcia, M. et al. (2008). “Radiative transfer revisited for emission lines in photon dominated regions”. In: A&A 485.1, pp. 127–136. DOI: [10.1051/0004-6361:200809440](https://doi.org/10.1051/0004-6361:200809440).
- Gould, R. J. and Salpeter, E. E. (1963). “The Interstellar Abundance of the Hydrogen Molecule. I. Basic Processes.” In: ApJ 138, p. 393. DOI: [10.1086/147654](https://doi.org/10.1086/147654).
- Guzmán, V. et al. (2011). “H₂CO in the Horsehead PDR: photo-desorption of dust grain ice mantles”. In: A&A 534, A49, A49. DOI: [10.1051/0004-6361/201117257](https://doi.org/10.1051/0004-6361/201117257).
- Habart, E. et al. (2005). “Density structure of the Horsehead nebula photo-dissociation region”. In: A&A 437.1, pp. 177–188. DOI: [10.1051/0004-6361:20041546](https://doi.org/10.1051/0004-6361:20041546).
- Herbst, E. and van Dishoeck, E. F. (2009). “Complex Organic Interstellar Molecules”. In: ARA&A 47.1, pp. 427–480. DOI: [10.1146/annurev-astro-082708-101654](https://doi.org/10.1146/annurev-astro-082708-101654).
- Hernández-Vera, C. et al. (2023). “The extremely sharp transition between molecular and ionized gas in the Horsehead nebula”. In: A&A 677, A152. DOI: [10.1051/0004-6361/202347206](https://doi.org/10.1051/0004-6361/202347206).
- Hollenbach, D. and Salpeter, E. E. (1971). “Surface Recombination of Hydrogen Molecules”. In: ApJ 163, p. 155. DOI: [10.1086/150754](https://doi.org/10.1086/150754).
- Joblin, C. et al. (2018). “Structure of photodissociation fronts in star-forming regions revealed by Herschel observations of high-J CO emission lines”. In: A&A 615, A129, A129. DOI: [10.1051/0004-6361/201832611](https://doi.org/10.1051/0004-6361/201832611).
- Le Bourlot, J. et al. (2012). “Surface chemistry in the interstellar medium. I. H₂ formation by Langmuir-Hinshelwood and Eley-Rideal mechanisms”. In: A&A 541, A76, A76. DOI: [10.1051/0004-6361/201118126](https://doi.org/10.1051/0004-6361/201118126).
- Le Petit, F. et al. (2006). “A Model for Atomic and Molecular Interstellar Gas: The Meudon PDR Code”. In: ApJS 164.2, pp. 506–529. DOI: [10.1086/503252](https://doi.org/10.1086/503252).
- Maillard, V. (2023). “Model of photo-evaporating fronts in star forming regions”. Theses. Université Paris sciences et lettres.
- Maillard, V., Bron, E., and Le Petit, F. (2021). “Dynamical effects of the radiative stellar feedback on the H I-to-H₂ transition”. In: A&A 656, A65, A65. DOI: [10.1051/0004-6361/202140865](https://doi.org/10.1051/0004-6361/202140865).
- Marconi, A. et al. (1998). “Near infrared spectra of the Orion bar”. In: A&A 330, pp. 696–710. DOI: [10.48550/arXiv.astro-ph/9710051](https://doi.org/10.48550/arXiv.astro-ph/9710051).
- Mathis, J. S., Mezger, P. G., and Panagia, N. (1983). “Interstellar radiation field and dust temperatures in the diffuse interstellar medium and in giant molecular clouds”. In: A&A 128, pp. 212–229.
- Menten, K. M. et al. (2007). “The distance to the Orion Nebula”. In: A&A 474.2, pp. 515–520. DOI: [10.1051/0004-6361:20078247](https://doi.org/10.1051/0004-6361:20078247).
- Pilbratt, G. L. et al. (2010). “Herschel Space Observatory. An ESA facility for far-infrared and submillimetre astronomy”. In: A&A 518, L1, p. L1. DOI: [10.1051/0004-6361/201014759](https://doi.org/10.1051/0004-6361/201014759).
- Röllig, M. et al. (2007). “A photon dominated region code comparison study”. In: A&A 467.1, pp. 187–206. DOI: [10.1051/0004-6361:20065918](https://doi.org/10.1051/0004-6361:20065918).
- Rybicki, G. B. and Lightman, A. P. (1979). *Radiative processes in astrophysics*.
- Schirmer, T. et al. (2020). “Dust evolution across the Horsehead nebula”. In: A&A 639, A144, A144. DOI: [10.1051/0004-6361/202037937](https://doi.org/10.1051/0004-6361/202037937).
- Schlafly, E. F. et al. (2014). “A Large Catalog of Accurate Distances to Molecular Clouds from PS1 Photometry”. In: ApJ 786.1, 29, p. 29. DOI: [10.1088/0004-637X/786/1/29](https://doi.org/10.1088/0004-637X/786/1/29).
- Stacey, G. J. et al. (2010). “A 158 μ m [C II] Line Survey of Galaxies at $z \sim 1-2$: An Indicator of Star Formation in the Early Universe”. In: ApJ 724.2, pp. 957–974. DOI: [10.1088/0004-637X/724/2/957](https://doi.org/10.1088/0004-637X/724/2/957).

- Tielens, A. G. G. M. and Hollenbach, D. (1985). “Photodissociation regions. I. Basic model.” In: ApJ 291, pp. 722–746. DOI: [10.1086/163111](https://doi.org/10.1086/163111).
- Warren Jr., W. H. and Hesser, J. E. (1977). “A photometric study of the Orion OB1 association. I. Observational data.” In: ApJS 34, pp. 115–206. DOI: [10.1086/190446](https://doi.org/10.1086/190446).
- Wolfire, M. G., Vallini, L., and Chevance, M. (2022). “Photodissociation and X-Ray-Dominated Regions”. In: *Annual Review of Astronomy and Astrophysics* 60. Volume 60, 2022, pp. 247–318. DOI: <https://doi.org/10.1146/annurev-astro-052920-010254>.
- Wu, R. et al. (2018). “Constraining physical conditions for the PDR of Trumpler 14 in the Carina Nebula”. In: A&A 618, A53, A53. DOI: [10.1051/0004-6361/201832595](https://doi.org/10.1051/0004-6361/201832595).

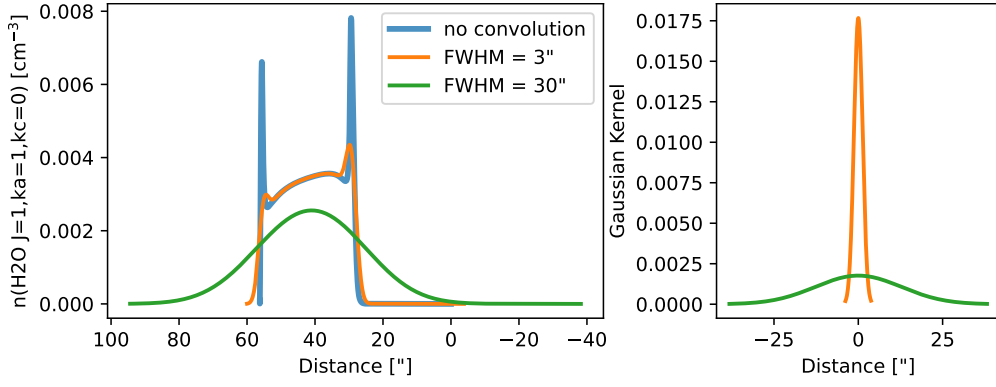


Figure 17: Illustration of the Convolution Process. The left panel shows the original line profile (blue) alongside the profiles convolved with Gaussian PSFs of resolutions 3'' (orange) and 30'' (green). The right panel shows the corresponding Gaussian PSFs, normalized and truncated at 3σ .

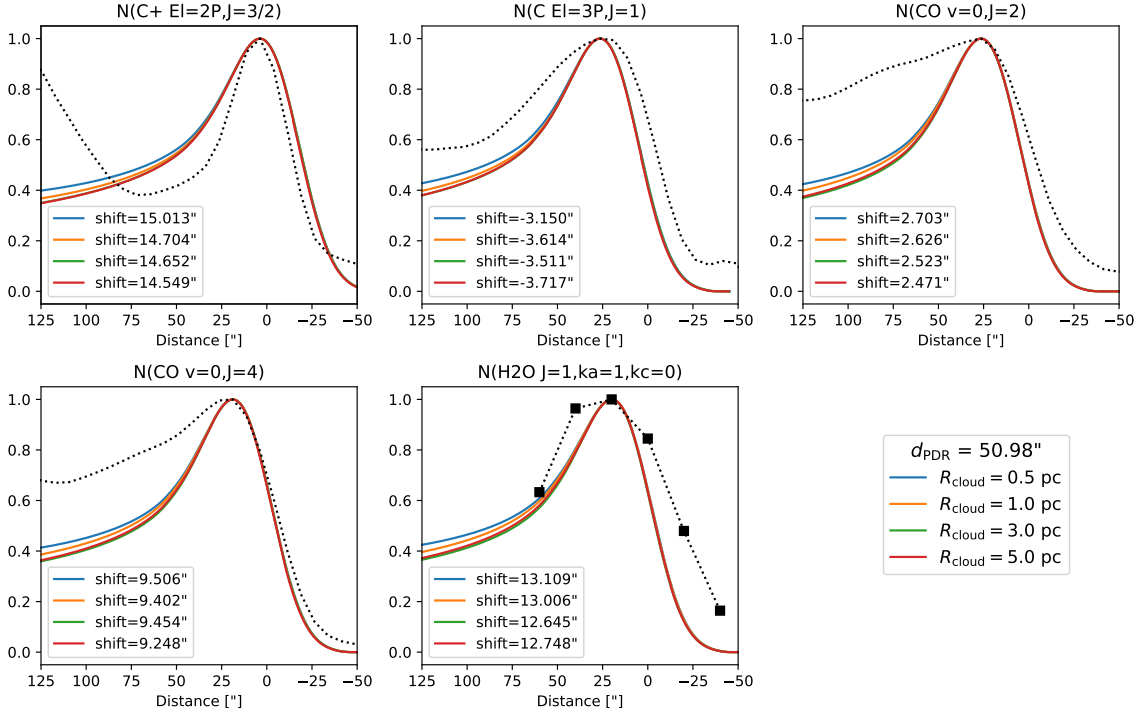


Figure 18: Comparison of normalized line profiles for different cloud radii: $R_{\text{cloud}} = 0.5$ pc (blue), 1.0 pc (orange), 3.0 pc (green), and 5.0 pc (red). The profiles are shifted to align with the peak locations in the observational data (dotted lines), with the corresponding shifts for each model indicated in the legend.